Transient growths of stable modes in riverbed dynamics

Transient growths of stable modes in riverbed dynamics

R. Vesipa, C. Camporeale, L. Ridolfi

Dept. Environmental, Land and Infrastructure Engineering, Politecnico di Torino, Corso Duca Abruzzi 24, 10129, Turin, Italy

PACS 47.20.Hw – Morphological instability
PACS 92.40.qh – Rivers
PACS 92.40.Gc – Erosion and sedimentation

Abstract – Fluvial bars are regular widespread bedforms that are characterized by vertical and transversal scales which are comparable with the stream depth and width, respectively. Although well-established linear and weakly nonlinear stability analysis have already been performed, no nonmodal analysis has been proposed yet. We here demonstrate the remarkable nonnormality of the operator that governs bar dynamics in large regions of the parameter space in fair agreement with our tests in flume experiments. This entails the occurrence of dramatic transient growths in the evolution of bed perturbations. Such algebraic growths suggest a novel explanation, through a purely linear process, of the progressive increase in the dominant bar wavelength that is observed in flume experiments and real rivers during bar inception.

Rivers exhibit a broad collection of striking morphological shapes, ranging from centimetric ripples to giant meanders, with an astonishing variety of patterns, such as dunes, bars and braided channels. These features have always attracted the interest of scientists because of their beauty and great engineering and environmental significance for society. In the last few decades, fluid dynamics has been crucial to explain the occurrence of geophysical patterns as the result of morphological instability processes driven by a free-surface stream [1, 2]. Nowadays, a gamut of theoretical models describe river patterns through the subtle use of the asymptotic stability analysis technique, in fair agreement with experimental data [3]. Nevertheless, several questions remain open. One of the most challenging concerns the possible occurrence of transient growths in regions of the parameter space in which the system is asymptotically stable (AS). In spite of their transience, such growths can be rather relevant, trigger nonlinear instabilities, and display significant timescales [4].

Basically, transient growths are due to nonmodal linear interactions and are related to the nonnormality of the eigenvector set. The nonmodal approach has been decisive in fluid mechanics to solve a number of open questions concerning shear-flow hydrodynamic instabilities [4–6]. Although rivers are the site of spectacular morphodynamic instabilities, only very recently the possible occurrence of transient growths has been demonstrated for river dunes [7] and one-dimensional bed waves [8]. We here focus on free bars, one of the most ubiquitous and impacting river morphologies, that develop when the width-to-depth aspect ratio, β, exceeds a critical threshold. They are slowly downstream migrating perturbations of the sediment bottom, and are characterized by a diagonal front, with horizontal and vertical length scales of the order of the channel width and the stream depth, respectively (see figure 1). Unlike previous studies, which were focused on the eigenvalue problem that determines the asymptotic fate of perturbations, in this Letter we tackle bar formation through an initial boundary problem approach. We demonstrate, through theory and experiments, that nonnormal transient growths very likely occur in rivers. Our results shed light on some unexplained aspects observed experimentally during the bar wavelength selection stage, and provide a novel tool to disentangle fluvial dynamics.

Let us consider a free-surface turbulent water stream flowing on a cohesionless bed of granular material. The local bed elevation, η, and the free-surface elevation, H, are defined with respect to the horizontal plane $\{s, n\}$, while $D{=}H-\eta$ is the local stream depth. Shallow water equations for the momentum, water and sediment mass balance are commonly adopted to describe bar dynamics [9] and, in dimensionless form, can be written as

$$\mathbf{U}_{,t} + \mathbf{U}\cdot\nabla\mathbf{U} + \nabla H + \beta\boldsymbol{\tau}D^{-1} = 0, \qquad (1)$$

$$D_{,t} + \nabla\cdot(\mathbf{U}D) + p\eta_{,t} = 0, \qquad \eta_{,t} + Q\nabla\mathbf{Q}_s = 0 \quad (2a, b)$$

Fig. 1: Picture of an alternate bar pattern in the Rhine River, near Vaduz, Liechtenstein (47°06′40″N, 9°31′02″E). The bar wavelength, λ, is shown; the arrow indicates the flow direction.

where the bulk velocity and stream depth have been used to make variables dimensionless. $\mathbf{U}\equiv\{U,V\}$ is the depth-averaged fluid velocity, $\boldsymbol{\tau}=C\mathbf{U}|\mathbf{U}|$ is the bottom shear stress vector, C is the friction factor, $\mathbf{Q_s}=\{\cos\delta,\sin\delta\}\Phi$ is the sediment bedload vector – where $\sin\delta=\boldsymbol{\tau_n}\ /\ |\boldsymbol{\tau}|$-$a\eta_{,n}$ and Φ is the total bedload magnitude –, Q is the ratio between the sediment and flow rate discharge scales, and $\nabla\equiv\{\partial_s,\partial_n\}$ (details on the closure relationships for C, Φ, Q, a are reported in the Appendix). Eqs. (1-2) are completed with the boundary conditions $V=\eta_{,n}=0$ at $n=\pm1$ which state impermeable and fixed lateral walls.

The time derivatives in (1) and (2a) have so far always been disregarded, under the hypothesis that the flow field instantly adjusts to the bed geometry and only the temporal derivative in the Exner equation (2b) has to be retained. However, this quasi-steady approximation is unsuitable for a transient analysis, in which the interactions among the time evolutions of all the perturbation components play a crucial role. Accordingly, we will keep all the time derivatives in the system (1-2).

Let us consider the generic physical variable $f(s,n,t)$. In order to address the stability of its uniform solution, f_0, it is customary to adopt the ansatz $f=f_0+\epsilon G(n)f_1(t)\mathrm{e}^{\mathrm{i}\alpha s}$ where $G(n)=\sin(\pi n/2)$ [except when multiplied by v_1 where it reads $G(n)=\cos(\pi n/2)$], $\epsilon\ll1$, and α is the longitudinal wave number of the perturbation.

A nonmodal analysis requires a physically relevant norm that summarizes the behavior of the whole system to be chosen [10]. In the present problem, this (dimensionless) energy is the sum of the kinetic energy, $K=(|u_1|^2+|v_1|^2)/2$ and the free surface, $P_s=|h_1|^2/2F^2$, and bed, $P_b=\xi|\eta_1|^2/2F^2$, potential energies. In such relations, the null potential has been set on the undisturbed water surface and $\xi=(1-p)R$, where R represents the submerged sediment density ($R\sim1.6$ for silicate sediments), p is the sediment porosity and F is the Froude number of the unperturbed state. In order to focus on transient growths of the energy related to the morphological instability, P_b, the other two energy components are penalized by a coefficient $c\ll1$. This approach was successfully used, and described in detail, in [7, 8] for the analysis of other kinds of morphodynamic instabilities. In this way, only the bed energy is actually taken into account. The total energy density of the perturbation is therefore equal to $E_M=||\boldsymbol{q}_M||^2$, where $||\cdot||^2$ is the l^2 norm and $\mathbf{q}_M=\sqrt{2}\left(u_1,v_1,h_1F^{-1},\eta_1(cF)^{-1}\sqrt{\xi}\right)/2$. In the sequel, when subscript $_M$ is omitted, the non-modified case $c=1$ is intended.

Upon linearization of (1)-(2), one obtains $\mathrm{d}\mathbf{q}_M/\mathrm{d}t=\mathbf{A}\mathbf{q}_M$, so that the matrix $\mathbf{A}$ fully describes the whole time evolution of $\mathbf{q}_M$, i.e., its asymptotic and transient behaviors (coefficients of matrix $\mathbf{A}$ are reported in the Appendix). The former only requires the analysis of the four eigenvalues, σ_i, the latter also calls for a nonnormal investigation of the eigenvectors.

In order to show the nonnormality of the eigenvector set of $\mathbf{A}$ we arrange them in columns in matrix $\mathbf{V}$ and compute the condition number, $\kappa=||\mathbf{V}||||\mathbf{V}^{-1}||$. This metric is a proxy of matrix singularity and, accordingly, $\kappa=1$ means orthogonality whereas $\kappa\gg1$ is a symptom of a high degree of nonnormality. Figures 2a,b report κ as a function of the dimensionless grain roughness, d_s and the Shield stress, $\theta=|\boldsymbol{\tau}|F^2/Rd_s$, for some exemplifying cases (both parameters d_s and θ affect the closure relationships). High values occur (of order 10^2) , especially for small values of θ and d_s. Nonnormal behavior of bar dynamics is therefore expected in fine sediment beds characterized by low slopes.

Let us consider marked points P_1 and P_2, reported in figure 2a, which are two particular AS cases, namely the least stable eigenvalue has a negative real part. Case P_1 (P_2) is characterized by high (low) condition number, which testifies a high (low) degree of nonnormality of operator $\mathbf{A}$. A well-defined overview of nonnormality of these two cases is achieved by means of pseudospectra, which are defined as

$$\Lambda_\omega(\mathbf{A})=\left\{z\in\mathbb{C}:\left\|(z\mathbf{I}-\mathbf{A})^{-1}\right\|\leq\omega^{-1}\right\},\qquad(3)$$

where $\omega\ll1$. If operator $\mathbf{A}$ is normal, the resolvent set is only large very close to the eigenvalues and the pseudospectrum is the union of circles of radius ω centered on the eigenvalues [as $\omega\to0$, (3) provides the spectrum Λ]. Instead, when the matrix is non-normal, the norm of the resolvent is also very large far away from the eigenvalues, and pseudospectra form a much larger set than in the case of a normal operator. These concepts are applied to cases P_1 and P_2 in figures 2c and 2d, respectively. The pseudospectrum portrait of case A confirms the high degree of nonnormality: it appears as a much larger set of complex numbers than the union of the ϵ-radius disks centered in the eigenvalues, whereas the quasi-normal behavior is confirmed for case P_2 by a pseudospectrum portrait which

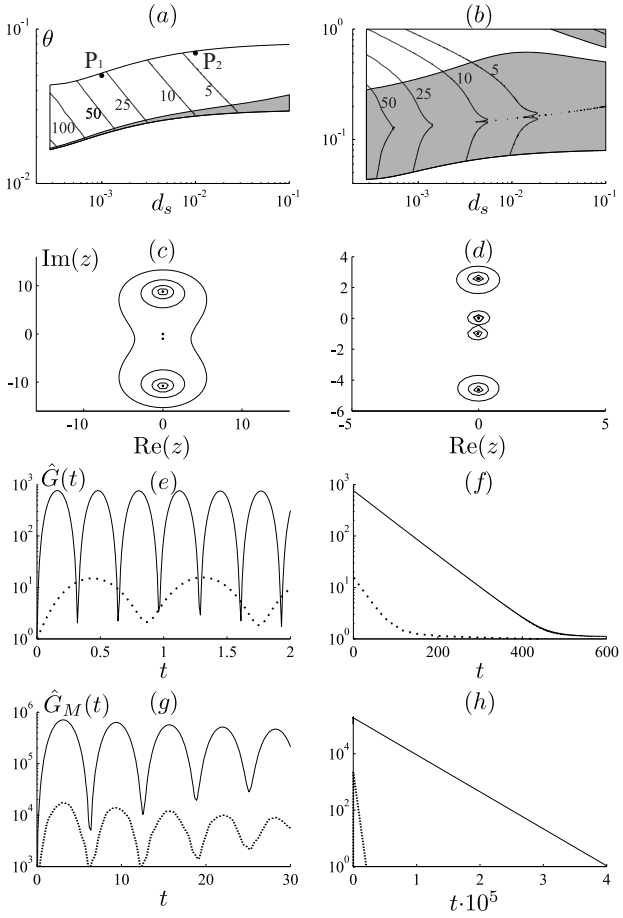

Fig. 2: (a,b) Contour lines of the surface $\kappa(d_s, \theta)$, for k=1 and β=5 in the region of bar occurrence. The shaded zones correspond to AU regions: plane (a) and dune-covered (b) bed. (c,d) Pseudospectra plots corresponding to cases P_1 and P_2 marked in panel (a), respectively, with ω=0.4, 0.2, 0.1, 0.05. (e,f) Growth functions plots for case P_1 (solid lines) and case P_2 (dotted lines): (e) transient behavior, (f) peak envelope of the long term behavior. (g,h) Like panels (e,f) but with the penalty coefficient $c = 10^{-6}$.

essentially coincides with the union of the circles centered on the eigenvalues.

More physical insight into the nonmodal behavior of bar dynamics is provided through an analysis of the growth function, $\hat{G}(t)$. This metric is defined as the upper envelope of the evolution, $G(t)$, of the normalized energy density for all possible initial conditions [4], namely,

$$\hat{G}(t) = \max_{\mathbf{q}_0} G(t) = \max_{\mathbf{q}_0} \frac{\|\mathbf{q}(t)\|^2}{\|\mathbf{q}_0\|^2} = \left\|e^{\mathbf{A}t}\right\|^2 \quad \forall \mathbf{q}_0, \qquad (4)$$

where $\mathbf{q}_0$ is the initial disturbance. Unlike an initial value problem, no particular structure of the initial disturbance has to be specified, and each possible evolution is explored. This is coherent with real cases in which a number of perturbations randomly excite the system.

An optimization procedure, based on singular value decomposition, can conveniently be used to evaluate the

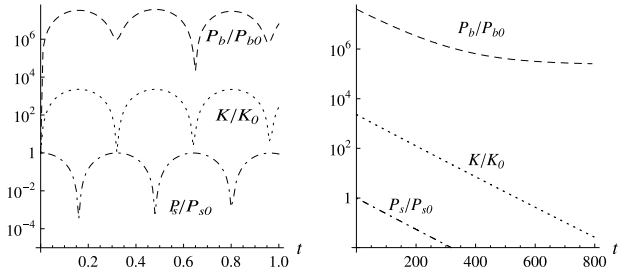

Fig. 3: (a) Time behavior of the different components of E_M scaled to their initial values, by using as initial condition the optimal morphodynamic initial condition, and data referring to case P_1. (b) Peak envelope at longer timescales.

growth function: observing that $\mathbf{AV} = \mathbf{V}\Lambda(\mathbf{A})$, it is possible to write $\hat{G}(t) = s^2 \left[\mathbf{V} \exp\left(t\Lambda(\mathbf{A})\right)\mathbf{V}^{-1}\right]$ where s is the maximum singular value [4]. The growth function behavior, with reference to cases P_1 and P_2, is plotted in figures $2e, f$. The operator with the highest condition number exhibits the largest transient growth, which is due to a purely linear mechanism.

The computation of the growth function is repeated for operator $\mathbf{A}_M$ in figures $2g, h$. The picture remains qualitatively the same, but larger transient growths occur (by a factor of 10^3), which are characterized by longer time scales (factor 500) and oscillations with longer periods (factor 10) than those observable for $\mathbf{A}$. The reason for these changes is that the amplifications are now ascribable to transient growths of the bed elevation, whose dynamics is characterized by longer timescales than those of the hydrodynamic modes.

It is now possible to evaluate the temporal evolution of the single energy components adopting the optimal initial condition that maximizes $\hat{G}(t)$ as the initial condition of the differential system. It should be noted that the modified operator $\mathbf{A}_M$ is only used to select the initial conditions that are prone to developing the greatest morphological transient growths, but the dynamics of the energy components is evaluated according to the actual $\mathbf{A}$ operator. The energy components, scaled to their initial value, are reported in figure 3. The growth rate of bed potential-energy is extremely high ($\sim 10^8$), compared to the growth rate of the kinetic energy ($10^3 - 10^4$). Therefore, the modified energy E_M allows one to select initial conditions whose corresponding evolutions of the perturbation are characterized by a temporary transfer of energy from hydrodynamic and free surface modes to the morphodynamic mode. As a consequence, the nonnormality of operator $\mathbf{A}$ can drive transient growths that can play a role in bar morphodynamics.

The previously detected remarkable nonnormality sheds light on a peculiar behavior that has been observed during wavelength selection in fluvial bars [11, 12], namely the progressive increment of the average bar wavelength till the asymptotic one is reached. In order to focus on this process, we performed new experiments devoted to

Table 1: Set of hydraulic parameters used in the six runs (in all runs channel width is equal to 500 mm).

RUN	θ	β	$10^2 \cdot d_s$	Q_l^*	$10^3 \cdot S$	$10^2 \cdot U_0^*$
	[-]	[-]	[-]	[l·s^{-1}]	[-]	[m/s]
a	0.087	15.4	2.8	2.5	4.0	31
b	0.081	20.8	3.7	1.7	5.0	28
c	0.081	20.8	3.7	1.7	5.0	28
d	0.095	24.8	4.5	1.5	7.0	30
e	0.090	24.3	4.4	1.5	6.5	29
f	0.089	18.9	3.4	2.0	5.0	30

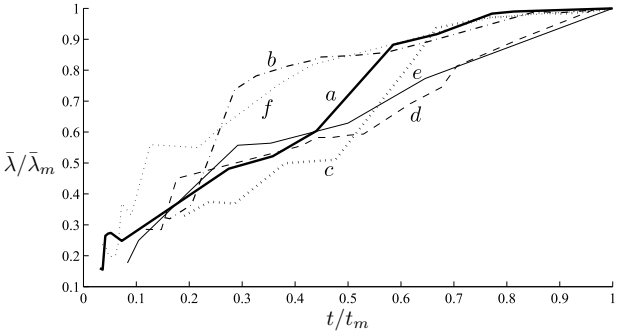

Fig. 4: Evolution of the flume-averaged wavelength over time for six experiments. Both the wavelength and time are scaled to the values that correspond to the occurrence of stable mature bars.

investigate the first stages of bar formation. The experiments were carried out in a sediment-fed flume 18 m long, 3 m wide, and 0.6 m deep. It was filled with sand, and was equipped with a scraper on a gantry, a sand feeder, the measurement systems, and a water supply system (see [13] for details). The sand used for the experiments had a specific weight of 2650 kg m^{-3}, a mean grain size of D_{50}=0.45 mm, and was moderately sorted, with a sorting index $I_s = 0.5(D_{84}/D_{50} + D_{50}/D_{16}) = 0.55$. The porosity and the hydraulic conductivity were 0.4 and $3 \cdot 10^{-4}$ m s^{-1}, respectively.

The sand scraper was used to obtain a flat surface with constant slope, the water level in the upstream stilling tank was then increased to supply the prescribed fluid discharge. After a short transitory (about one minute), during which the flowing water filled the entire flume, we observed a uniform flow in the channel. The flow was maintained until the bar pattern reached its asymptotic equilibrium condition (i.e., no significant evolution of the wavelength or amplitude of the bars were observed). Four cameras, fixed above the flume, recorded the bed configuration with time step equal to 2.5 minutes. Because of the lack of suspended sediments, the bar pattern was acquired with pixel-precision, which corresponds to 1-1.5 mm, depending on the run. At each sampling time t_j, we measured the N_j wavelengths, $\lambda_{i,j}$ $(i = 1, ..., N_j)$ and obtained the mean value $\bar{\lambda}_j = (\sum_i \lambda_{i,j})/N_j$. During the very preliminary stages, the camera resolution, the shadows and the light reflection due to the water free surface made the identification of the bar front difficult in the aerial pictures taken from the laboratory ceiling. In order to overcome this problem, the bar fronts were detected (thanks to better illumination conditions) by monitoring the bedform evolution through a direct observation performed standing beside the channel.

Six runs were performed and table 1 reports the corresponding experimental setups. In particular, the key quantities that regulate bar dynamics – which are usually chosen as control parameters in theoretical analysis [14], numerical simulations [15] and field and flume experiments [12] – are the aspect ratio β, the dimensionless sediment diameter d_s and the Shields parameter θ.

Figure 4 shows the results of our laboratory experiments about the temporal evolution of the average bar wavelength: all runs exhibit a clear progressive increment of the wavelength till the asymptotic one is reached. So far this behavior has generically been ascribed to nonlinearities, but no further explanation of their role has been offered. More importantly, this interpretation contrasts with the fact that the asymptotic wavelength is well-described by a linear theory, thus the following open question arises: Why is the linear theory successful in the long term but should fail to describe bar inception when the disturbances are smaller than the asymptotic ones? We here provide a possible answer which is supported with laboratory evidence.

Figures 2 and 3 prove that the nonnormality of the fluvial dynamical system leads to a significant transfer of energy among the hydrodynamic modes and the morphodynamic one. This drives remarkable transient growths of the bed potential energy even for asymptotically stable wavenumbers. As hydrodynamic modes are involved in such an energy transfer, the typical timescales of transient behavior are expected to be lower than the time that the asymptotically unstable (AU) bed perturbations need to grow, to became mature bars, and to dominate the dynamics. It follows that the dynamical system will show (at least in its linear behavior) different dominant wavelengths at different times: the wavelengths activated by the transient exchange of energy between hydrodynamic and morphodynamics perturbations will occur first, then the AU wavelengths will start to emerge until the most AU model remains the only one. If the AU wave is longer than those exhibiting the greatest transient growths, then the dynamical system will exhibit a wavelength that grows in time. According to this picture, purely linear mechanisms are therefore able to explain the experimental observations. Nonlinear processes are surely necessary for the saturation of exponential disturbance growth and they can alter the quantitative details of the linear picture, but the core of the wavelength evolution should be dictated by purely linear wave interactions.

Figure 5 confirms this explanation. It shows the evolution of the growth function $\hat{G}_M(\alpha)$ for a set of parameters in the range explored in our experiments. The fig-

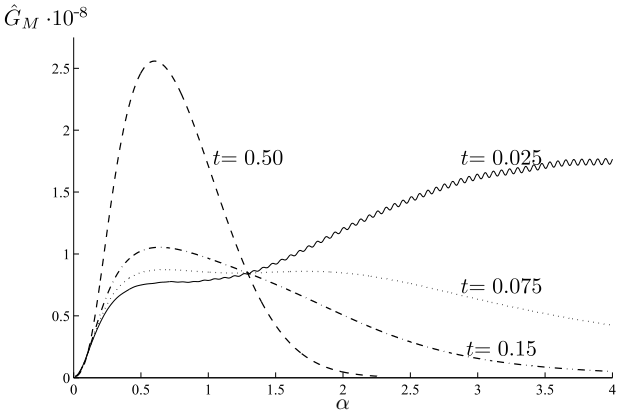

Fig. 5: Behavior of $\hat{G}_M$ as a function of the wave number, α, for fixed times (Run 'a', β=15.4, θ=0.087, $d_s = 0.028$, c=10^{-6}).

ure clearly shows that the AU wavenumbers do not dominate the dynamics at the first stages. On the contrary, and in agreement with the experiments, a large family of disturbances with lower wavelengths exhibits very strong nonnormality-induced transient amplifications that overcome the AU waves. Then, while time increases, the wavenumber for which $\hat{G}_M$ is maximum decreases (i.e., the wavelength increases), and the process continues until the peak corresponding to AU, α_{asy}, begins to prevail and the amplification of the AS waves tends to decay. This process continues until the transient growths have completely dissipated and only the AU modes survive and dominate the (linearized) bar dynamics. If the bar dynamical system had been normal, the scenario depicted in figure 5 would be totally different as the AU waves would have dominated from the initial times.

We believe that the huge realm of environmental morphological patterns involves several nonnormal dynamical systems, that could be explored by means of a non-modal analysis. One of the most typical river morphologies, namely bars, has here been investigated in order to demonstrate this fact. We have demonstrated that non-negligible eigenvector nonnormality is ubiquitous in the parameter space and remarkable transient growths of asymptotically stable modes are therefore possible. This has allowed the wavelength dynamics that occur during bar inception to be explained only by means of linear wave interactions. The failure of previous analysis to justify the presence of short-lived waves with different celerities is therefore due neither to nonlinearities – which certainly play a role in the saturation process – nor to model drawbacks, but rather to the mathematical tools adopted for the analysis.

Appendix 1: Closure relation. – The drag coefficient C used to evaluate the bottom shear stress can be expressed as $C = [6+2.5\ln(D/2.5d_s)]^{-2}$ for unperturbed flat bed [16] and as $C = [6+2.5\ln(\theta' D/\theta 2.5d_s)]^{-2}\,\theta/\theta'$, for dune covered bed [18], where $\theta' = 0.06+0.4\theta^2$. The Chabert's criteria [17] is adopted to distinguish a plane bed low regime from dune covered bed regime. The limit for a ripple bed regime is defined by the Engelund's diagram [18].

The total sediment flow magnitude Φ can be evaluated through the Meyer-Peter and Muller formula $\Phi = 8(\theta-\theta_c)^{3/2}$ in the case of plane bed [19] or through the relation $\Phi = 0.05\theta^{5/2}/C$ for dune covered bed [18]. The threshold value of the Shields parameter for sediment motion inception, θ_c, is expressed by means of the Brownlie's relation [20]. It also holds true $a = r/\beta\sqrt{\theta}$ where r is an experimental constant for which the value 0.3 is suggested [14,21] and $Q = d_s^*\left[(\rho_s/\rho-1)\,g d_s^*\right]^{1/2}/(1-p)\,D_0^* U_0^*$.

Appendix 2: Algebraic operator A. – The operator describing the time evolution of an initial perturbation reads

$$\mathbf{A} = \frac{-\mathrm{i}k}{F_0^{-3}}\begin{bmatrix} a_{11} & 0 & a_{13} & a_{14} \\ 0 & a_{22} & a_{23} & 0 \\ a_{31} & a_{32} & a_{33} & a_{34} \\ a_{41} & a_{42} & a_{43} & a_{44} \end{bmatrix}, \tag{5}$$

where

$$a_{11} = \tfrac{k-\mathrm{i}\chi_0\hat{s}_1}{kF_0^3},\ a_{13} = \tfrac{1}{F_0^2} - \tfrac{\mathrm{i}\chi_0(\hat{s}_2-1)}{k},\ a_{14} = \tfrac{\mathrm{i}\chi_0(\hat{s}_2-1)}{kF_0^2\sqrt{\xi}},$$
$$a_{22} = \tfrac{k-\mathrm{i}\chi_0}{kF_0^3},\ a_{23} = \tfrac{-\mathrm{i}\pi}{2kF_0^2},\ a_{31} = \tfrac{\hat{f}_1 Q_0\Phi_0+1}{F_0^6},$$
$$a_{32} = \tfrac{\mathrm{i}\pi(Q_0\Phi_0+1)}{2kF_0^6},\ a_{33} = \tfrac{\hat{f}_2 Q_0\Phi_0+1}{F_0^3},$$
$$a_{34} = \tfrac{-4\hat{f}_2 Q_0\Phi_0 k - k - \mathrm{i}\pi^2 Q_0\Phi_0\hat{R}}{4kF_0^5\sqrt{\xi}},\ a_{41} = \tfrac{\hat{f}_1 Q_0\Phi_0\sqrt{\xi}}{\bar{p}F_0^4},$$
$$a_{42} = \tfrac{\mathrm{i}\pi Q_0\Phi_0\sqrt{\xi}}{2\bar{p}kF_0^4},\ a_{43} = \tfrac{\hat{f}_2 Q_0\Phi_0\sqrt{\xi}}{\bar{p}F_0},\ a_{44} = \tfrac{-Q_0\Phi_0(\mathrm{i}\pi^2\hat{R}+4\hat{f}_2 k)}{4\bar{p}kF_0^3}.$$

In the previous relations

$$\hat{s}_1 = 2\,(1-C_T)^{-1},\ \hat{s}_2 = C_D\,(1-C_T)^{-1},\ \chi_0 = \beta C_0,$$
$$\bar{p} = (1-p),\ \hat{f}_1 = \tfrac{2\Phi_t}{1-C_T},\ \hat{f}_2 = \Phi_D + \tfrac{C_D\Phi_t}{1-C_T},\ \hat{R} = \tfrac{r}{\beta\sqrt{\theta_0}},$$
$$C_D = \tfrac{1}{C_0}\tfrac{\partial C}{\partial D},\ C_T = \tfrac{\theta_0}{C_0}\tfrac{\partial C}{\partial \theta},\ \Phi_D = \tfrac{1}{\Phi_0}\tfrac{\partial \Phi}{\partial D},\ \Phi_T = \tfrac{\theta_0}{\Phi_0}\tfrac{\partial \Phi}{\partial \theta}.$$

REFERENCES

[1] Huppert H., *J. Fluid Mech.*, **173** (1986) 557.
[2] Camporeale C. and Ridolfi L., *Phys. Rev. Lett.*, **108** (2012) 238501.
[3] Seminara G., *Annu. Rev. Fluid Mech.*, **42** (2010) 43.
[4] Trefethen L. and Embree M., *Spectra and Pseudospectra*, edited by Princeton Univ. Press 2001.
[5] Trefethen L., Trefethen A., Reddy S. and Driscoll T., *Science*, **261** (1993) 578.
[6] Schmid P. and Henningson D., *Stability and Transition in Shear Flows*, edited by Springer 2001.
[7] Camporeale C. and Ridolfi L., *Phys. Fluids*, **23** (2011) 104102.
[8] Camporeale C. and Ridolfi L., *Water Resour. Res.*, **45** (2009) W08418.
[9] Blondeaux P. and Seminara G., *J. Fluid Mech.*, **157** (1985) 449.
[10] Olsson P. and Henningson D., *Stud. Appl. Math.*, **94** (1995) 183.

[11] Fujita Y. and Muramoto Y., *Bulletin of the Disaster Prevention Research Institute*, Vol. **35** 1985.
[12] Lanzoni S., *Water Resour. Res.*, **36** (2000) 3337.
[13] Visconti F., Camporeale C. and Ridolfi L., *J. Geophys. Res.*, **115** (2010) F04042.
[14] Colombini M., Seminara G. and Tubino M., *J. Fluid Mech.*, **181** (1987) 213.
[15] Defina A., *Water Resour. Res.*, **39(4)** (2003) 1.
[16] Einstein H. A., *Technical Report 1026*, edited by U.S. Dept. of Agricolture 1950.
[17] Chabert J. and Chauvin J. L., *Technical Report 4*, edited by Cen. Rech. ess. Chatou 1963.
[18] Engelund F. and Hansen E., *A Monograph on Sediment Transport in Alluvial Streams*, edited by Danish Technical Press, Denmark 1967.
[19] Chien N., *Trans. ASCE*, **121** (1956) 833.
[20] Brownlie W. R., *Technical Report 43*, edited by W.M. Keck Laboratory of Hydraulics and Water Resources, California Institute of Technology 1981.
[21] Olesen K.W., *River Meandering: Proceeding of the Conference on rivers, 1983, New Orleans*, edited by ASCE 1983, p. 873.